

1 **Rheologic constraints on the upper mantle from five years of**
2 **postseismic deformation following the El Mayor-Cucapah**
3 **earthquake**

4 **T. T. Hines¹, E. A. Hetland¹**

5 ¹Department of Earth and Environmental Sciences, University of Michigan, Ann Arbor, Michigan, USA.

6 **Key Points:**

- 7 • = enter point 1 here =
8 • = enter point 2 here =
9 • = enter point 3 here =

10 **Abstract**

11 Five years of postseismic deformation following the Mw7.2 El Mayor-Cucapah earthquake re-
 12 veals transient deformation that decays back to its pre-earthquake trend after about three years
 13 at epicentral distances greater than ~ 200 km. At closer distances, the rapid transience decays
 14 to a sustained rate which exceeds its pre-earthquake trend. We attempt to determine the mech-
 15 anisms driving this deformation, where we consider afterslip at seismogenic depths and vis-
 16 coelastic relaxation in the lower crust and upper mantle as candidate mechanisms. We find that
 17 early, rapid, near-field deformation can be explained with afterslip on the fault that ruptured
 18 coseismically, while the later, sustained, near-field deformation can be explained with either
 19 continued afterslip in an effectively elastic lower crust, or lower crustal viscoelastic relaxation
 20 with a steady-state viscosity of $\sim 10^{19}$ Pa s. The trend in far-field deformation is best explained
 21 with a transient viscosity of $\sim 10^{18}$ Pa s in the upper mantle. We argue that a transient rhe-
 22 ology in the mantle is preferable over a Maxwell rheology because it better predicts the de-
 23 cay in postseismic deformation, and also because it does not conflict with the generally higher,
 24 steady-state viscosities inferred from studies of geophysical processes occurring over longer
 25 time-scales.

26 **1 Introduction**

27 Ground deformation in the years following a large (\gtrsim Mw7) earthquake provides insight
 28 into the mechanical behaviour of the crust and upper mantle. It has long been recognized that
 29 interpretations of postseismic deformation can be ambiguous because multiple postseismic de-
 30 formation mechanisms can have qualitatively similar surface expressions [e.g. Savage, 1990].
 31 Owing to the dense geodetic network deployed throughout the 2000s as part of the Plate Bound-
 32 ary Observatory, the postseismic deformation following the April 4, 2010, Mw7.2 El Mayor-
 33 Cucapah earthquake in Baja California was observed at more GPS stations than any other earth-
 34 quake in California to date. With such a large collection of data, we attempt to discern the mech-
 35 anisms driving postseismic deformation following the El Mayor-Cucapah earthquake, where
 36 we consider both afterslip and viscoelastic relaxation in the lower crust and upper mantle as
 37 candidate mechanisms.

38 Previous studies which have modelled postseismic deformation following the El Mayor-
 39 Cucapah earthquake include Pollitz *et al.* [2012], Gonzalez-Ortega *et al.* [2014], Spinler *et al.*
 40 [2015], and Rollins *et al.* [2015]. Of these studies, Gonzalez-Ortega *et al.* [2014] and Rollins
 41 *et al.* [2015] have attempted to describe the postseismic deformation with afterslip in an elas-
 42 tic half-space. Gonzalez-Ortega *et al.* [2014] described five months of postseismic deforma-
 43 tion, observed by InSAR and GPS within ~ 50 km rupture, with afterslip and contraction on
 44 the coseismically ruptured fault. Gonzalez-Ortega *et al.* [2014] noted that their preferred model
 45 underestimated the GPS displacements for stations $\gtrsim 25$ km from the rupture and suggested
 46 that it could be the result of unmodelled viscoelastic relaxation. Using only continuous GPS
 47 stations, which are mostly north of the rupture zone, Rollins *et al.* [2015] found that three years
 48 of postseismic deformation can be adequately explained by afterslip, albeit with an implau-
 49 sibly large amount of slip inferred on the least constrained, southern-most fault segment. Here,
 50 we suggest the afterslip inferred by Rollins *et al.* [2015] may have been acting as a proxy for
 51 distributed relaxation in the upper mantle.

52 Pollitz *et al.* [2012], Rollins *et al.* [2015] and Spinler *et al.* [2015] have explored viscoelas-
 53 tic relaxation in the lower crust and upper mantle as a potential postseismic deformation mech-
 54 anism. The rheology of the crust and mantle is largely unknown and so modelling postseis-
 55 mic deformation with viscoelastic relaxation requires one to assume a rheologic model and
 56 then find the best fitting rheologic parameters. The inference of these rheologic parameters is
 57 a computationally expensive non-linear inverse problem which is typically approached with
 58 a forward modelling grid search method. Consequently, a simplified structure for the Earth must
 59 be assumed in order to minimize the number of rheologic parameters that need to be estimated.
 60 For example, it is commonly assumed that the lower crust and upper mantle are homogeneous,

Maxwell viscoelastic layers, which may be too simplistic for postseismic studies [Riva and Govers, 2009; Hines and Hetland, 2013]. To further reduce the dimensions of the model space, it is also necessary to make simplifying assumptions about the nature of afterslip. For example, one can assume a frictional model for afterslip and parametrize afterslip in terms of the unknown rheologic properties of the fault [e.g. Johnson *et al.*, 2009; Johnson and Segall, 2004]. One can also assume that afterslip does not persist for more than a few months and then model the later postseismic deformation assuming it to be the result of only viscoelastic relaxation [e.g. Pollitz *et al.*, 2012; Spinler *et al.*, 2015]. However, postseismic afterslip in similar tectonic settings has been observed to persist for decades following earthquakes [Çakir *et al.*, 2012; Cetin *et al.*, 2014]. Indeed, the preferred viscoelastic model from Pollitz *et al.* [2012] significantly underestimates deformation in the Imperial Valley, which could be indicative of unmodelled continued afterslip. Neglecting to allow for sustained afterslip as a postseismic mechanism could then lead to biased inferences of lithospheric viscosities.

In this study, we perform a kinematic inversion for fault slip, allowing it to persist throughout the postseismic period, while simultaneously estimating the viscosity of the lower crust and upper mantle. We use the method described in Hines and Hetland [2016] to create an initial model of the fault slip and effective viscosity necessary to describe the early postseismic deformation. Our initial model describes the first 0.8 years of postseismic deformation following the El Mayor-Cucapah earthquake. We then use the inferred effective viscosity structure from the initial model to create a suite of postseismic models to explain the five years of postseismic data available to date. Of the suite of models tested, we find that postseismic deformation following the El Mayor-Cucapah earthquake can be explained with a combination of afterslip on a fault segment running through the Sierra Cucapah, a Zener rheology in the upper mantle with a transient viscosity that decays from 5×10^{18} Pa s to 1×10^{18} Pa s at 120 km depth, and a relatively stronger lower crust.

2 Data Processing

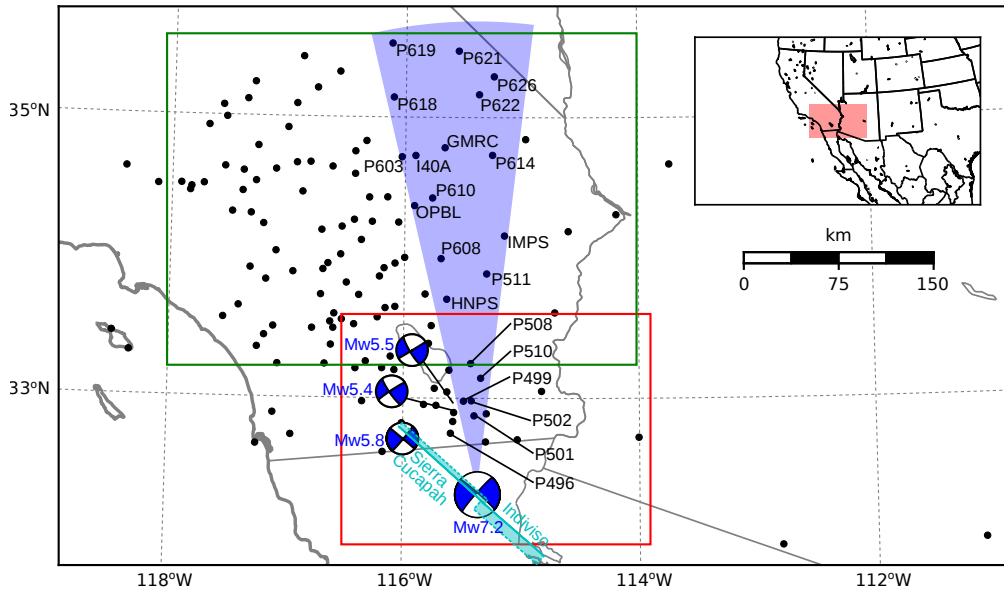
We use continuous GPS position time series provided by University Navstar Consortium (UNAVCO) for stations within a 400 km radius about the El Mayor-Cucapah epicentre. We collectively describe the coseismic and postseismic displacements resulting from the El Mayor-Cucapah earthquake as $u_{\text{post}}(t)$. We consider the GPS position time series $u_{\text{obs}}(t)$ to be the combination of $u_{\text{post}}(t)$, secular tectonic deformation, annual and semi-annual oscillations, and coseismic offsets from significant earthquakes over the time span of this study. The June 14, 2010, Mw5.8 Ocotillo earthquake and the Brawley swarm, which included an Mw5.5 and an Mw5.4 event on August 26, 2012, (Figure 1) are the only earthquakes that produced noticeable displacements in any of the time series. We treat the displacements resulting from the Brawley swarm as a single event because the daily solutions provided by UNAVCO cannot resolve the separate events. Although the Ocotillo earthquake had its own series of aftershocks [Hauksson *et al.*, 2011], neither the Ocotillo earthquake nor the Brawley swarm produced detectable postseismic deformation. We model displacements resulting from these events with only a Heaviside function, $H(t)$, describing the coseismic offsets. We then model $u_{\text{obs}}(t)$ as

$$u_{\text{obs}}(t) = u_{\text{pred}}(t) + \epsilon, \quad (1)$$

where

$$\begin{aligned} u_{\text{pred}}(t) = & u_{\text{post}}(t)H(t - t_{\text{emc}}) + c_0 + c_1 t + \\ & c_2 \sin(2\pi t) + c_3 \cos(2\pi t) + c_4 \sin(4\pi t) + c_5 \cos(4\pi t) + \\ & c_6 H(t - t_{\text{oc}}) + c_7 H(t - t_{\text{bs}}). \end{aligned} \quad (2)$$

In the above equations, t_{emc} , t_{oc} and t_{bs} are the times of the El Mayor-Cucapah earthquake, Ocotillo earthquake, and the Brawley swarm, respectively, c_0 through c_7 are unknown coefficients, and ϵ is the observation noise. We only estimate jumps associated with the Ocotillo earthquake and Brawley swarm for stations within 40 km of their epicentres.



86 **Figure 1.** Map of the region considered in this study. The large focal mechanism is for the El Mayor-
 87 Cucapah earthquake and the three small focal mechanisms are for the Ocotillo earthquake and the two main
 88 shocks during the Brawley swarm. The black dots indicate the locations of GPS stations used in this study.
 89 The fault geometry used in this study is shown in cyan where dashed lines indicate buried edges of the fault
 90 segments. The green and red boxes demarcate the extent of the near-field and far-field maps (Figures 4 and 5).
 91 Stations within the blue sector, which highlights the area within 10° of the El Mayor-Cucapah P axis, are used
 92 in Figures 7, 10, and 14

98 Stations which recorded displacements that clearly cannot be described by the aforementioned
 99 processes are not included in our analysis. This includes stations in the Los Angeles
 100 basin, where anthropogenic deformation can be larger than the postseismic signal that we are
 101 trying to estimate [Bawden *et al.*, 2001; Argus *et al.*, 2005]. In order to ensure an accurate es-
 102 timation of the secular deformation, we only use stations that were installed at least six months
 103 prior to El Mayor-Cucapah earthquake. Several GPS stations were installed after the El Mayor-
 104 Cucapah earthquake to improve the spatial resolution of postseismic deformation [Spinler *et al.*,
 105 2015]. Although it would be possible to subtract secular velocities derived from elastic block
 106 models [e.g. Meade and Hager, 2005] from velocities recorded at the newly installed stations
 107 to get an estimate of postseismic velocities, we do not do so here. We use coseismic and post-
 108 seismic displacements, rather than velocities, in our inverse method described in Section 3. We
 109 use displacements because estimating velocities from an already noisy displacement time se-
 110 ries can introduce significant uncertainties depending on exactly how the estimation is done.
 111 This choice prevents us from using the newly installed stations in Baja California for our anal-
 112 ysis.

113 The October 16, 1999, Mw7.1 Hector Mine earthquake, which occurred \sim 270 km north
 114 of the El Mayor-Cucapah epicentre, produced transient postseismic deformation which we do
 115 not wish to model, either mechanically or through empirical line fitting. We thus restrict our
 116 analysis to deformation observed six years after the Hector Mine earthquake, which is when
 117 postseismic velocities at sites proximal to the Hector Mine epicentre are approximately con-
 118 stant [Savage and Svare, 2009]. When appraising our model fit in Section 3, we see some sys-
 119 tematic residuals in the vicinity of the Hector Mine epicentre, which may be the result of er-
 120 rors in the assumption that the trend in Hector Mine postseismic deformation is linear after
 121 six years.

Studies of postseismic deformation typically assume a parametric form for $u_{\text{post}}(t)$, such as one with a logarithmic or exponential time dependence [e.g. Savage *et al.*, 2005]. However, by assuming a logarithmic or exponential form of $u_{\text{post}}(t)$ we run the risk of over fitting the GPS time series and inferring a non-existent postseismic signal. We therefore do not assume any parametric form for $u_{\text{post}}(t)$ and rather treat it as integrated Brownian motion, so that

$$\dot{u}_{\text{post}}(t) = \sigma^2 \int_0^t w(s) ds, \quad (3)$$

where $w(t)$ is white noise and the variance of $\dot{u}_{\text{post}}(t)$ increases linearly with time by a factor of σ^2 . We use a Kalman filtering approach to estimate $u_{\text{post}}(t)$ and the unknown parameters in eq. (2). In the context of Kalman filtering, our time varying state vector is

$$\mathbf{X}(t) = [u_{\text{post}}(t), \dot{u}_{\text{post}}(t), c_0, \dots, c_7] \quad (4)$$

and eq. (2) is the observation function which maps the state vector to the GPS observations. We initiate the Kalman filter by assuming a prior estimate of $\mathbf{X}(t)$ at the first time epoch, denoted $\mathbf{X}_{1|0}$, which has a sufficiently large covariance, denoted $\Sigma_{1|0}$, to effectively make our prior uninformed. For each time epoch t_i , Bayesian linear regression is used to incorporate GPS derived estimates of displacement with our prior estimate of the state $\mathbf{X}_{i|i-1}$ to form a posterior estimate of the state $\mathbf{X}_{i|i}$, which has covariance $\Sigma_{i|i}$. We then use the posterior estimate of the state at time t_i to form a prior estimate of the state at time t_{i+1} through the transition function

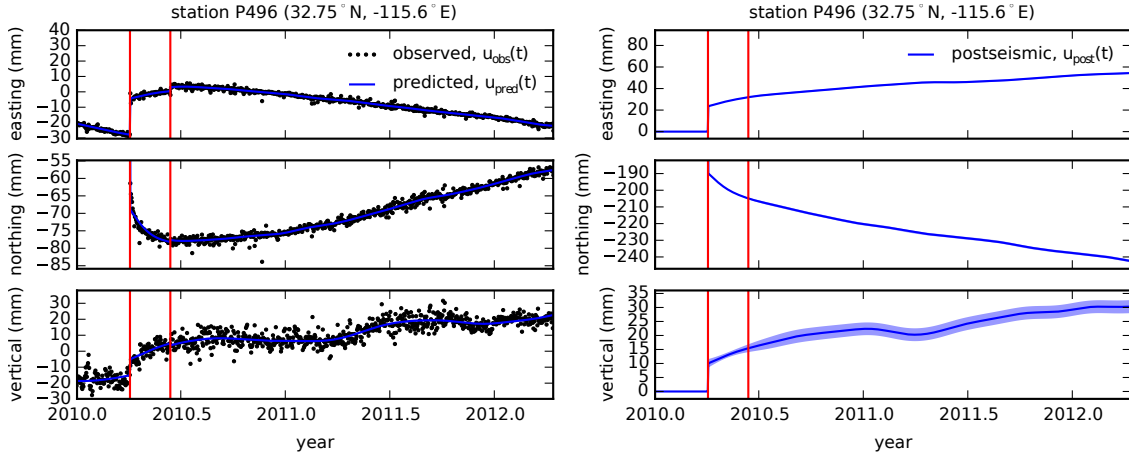
$$\mathbf{X}_{i+1|i} = \mathbf{F}_{i+1} \mathbf{X}_{i|i} + \delta_{i+1}, \quad (5)$$

where

$$\mathbf{F}_{i+1} = \begin{bmatrix} 1 & (t_{i+1} - t_i) & \mathbf{0} \\ 0 & 1 & \mathbf{0} \\ \mathbf{0} & \mathbf{0} & \mathbf{I} \end{bmatrix} \quad (6)$$

and δ_{i+1} is the process noise, which has zero mean and covariance described by

$$\mathbf{Q}_{i+1} = \sigma^2 \begin{bmatrix} \frac{(t_{i+1}-t_i)^3}{3} & \frac{(t_{i+1}-t_i)^2}{2} & \mathbf{0} \\ \frac{(t_{i+1}-t_i)^2}{2} & (t_{i+1} - t_i) & \mathbf{0} \\ \mathbf{0} & \mathbf{0} & \mathbf{0} \end{bmatrix}. \quad (7)$$



146 **Figure 2.** Left panels show GPS time series from UNAVCO (black) and the predicted displacement (blue)
 147 from eq. (2) for a near-field station. Red lines indicate the times of the El Mayor-Cucapah and Ocotillo earth-
 148 quakes. The right panels show estimated coseismic and postseismic displacements, u_{post} , which are extracted
 149 from the predicted displacements. The 68% confidence interval is shown in light blue.

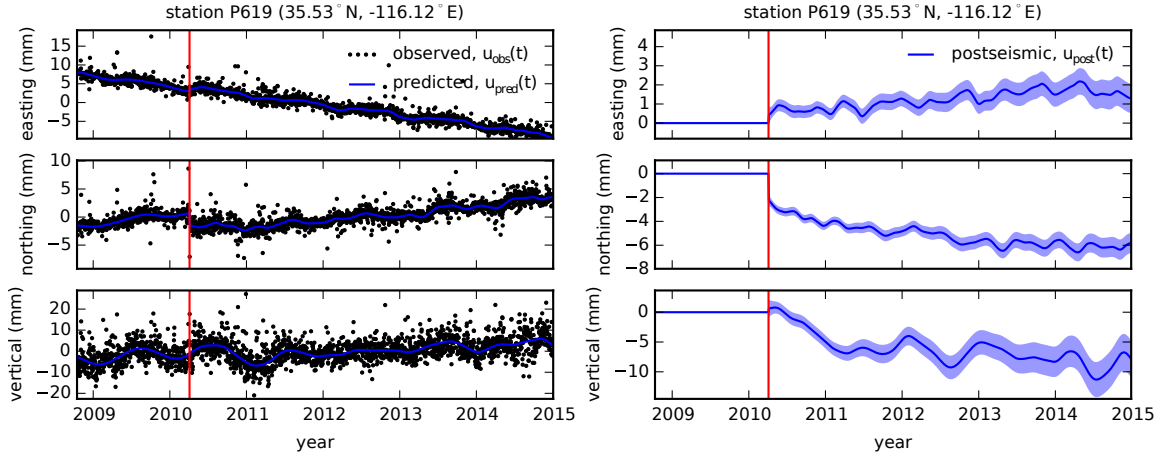
The covariance of the new prior state, $\mathbf{X}_{i+1|i}$, is then described by

$$\Sigma_{i+1|i} = \mathbf{F}_{i+1}\Sigma_{i|i}\mathbf{F}_{i+1}^T + \mathbf{Q}_{i+1}. \quad (8)$$

122 This process is repeated for each of the N time epochs at which point we use Rauch-Tung-
 123 Striebel smoothing [Rauch *et al.*, 1965] to find $\mathbf{X}_{i|N}$, which is an estimate of the state at time
 124 t_i that incorporates GPS observation for all N time epochs. Our final estimates of $u_{\text{post}}(t)$
 125 are used in subsequent analysis, while the remaining components of the state vector are con-
 126 sidered nuisance parameters. In the interests of computational tractability, we down sample
 127 our smoothed time series from daily solutions down to weekly solutions.

128 The smoothness of $u_{\text{post}}(t)$ is controlled by the chosen value of σ^2 , which describes how
 129 rapidly we expect postseismic displacements to vary over time. Setting σ^2 equal to zero will
 130 effectively result in modelling $u_{\text{post}}(t)$ as a straight line which is insufficient to describe the
 131 expected transient behaviour in postseismic deformation. The other end member, where σ^2 is
 132 infinitely large, will result in $u_{\text{pred}}(t)$ over fitting the data. While one can use a maximum like-
 133 lihood based approach for picking σ^2 [e.g. Segall and Mathews, 1997], we instead take a sub-
 134 jective approach and choose a value for σ^2 that is just large enough to faithfully describe the
 135 observed deformation at the most near-field station in our study, P496, which exhibits the most
 136 pronounced rapid changes in velocity. This ensures that σ^2 will be sufficiently large so that
 137 our estimate of $u_{\text{post}}(t)$ does not smooth out potentially valuable postseismic signal at the re-
 138 maining stations. We find that using $\sigma^2 = 0.05\text{m}^2/\text{yr}^3$ adequately describe all but the first
 139 week of postseismic deformation at station P496, which gets incorporated into our estimate
 140 of coseismic displacements (Figure 2). We assume that the first week of deformation is over-
 141 whelmingly the result of afterslip and this afterslip is lumped into our estimates of coseismic
 142 slip. Freed *et al.* [2007] noted that postseismic deformation can be observed at distances greater
 143 than 200 km from the Hector Mine earthquake and, after filtering the time series for stations
 144 up to 400 km from the El Mayor-Cucapah epicentre, we also clearly see far reaching postseis-
 145 mic transient deformation (Figure 3).

151 It is important to note that the shown uncertainties in $u_{\text{post}}(t)$ do not account for the non-
 152 negligible epistemic uncertainty in eq. (2). For example, we assume a constant rate of secu-
 153 lar deformation, which appears to be an appropriate approximation for all but perhaps the sta-
 154 tions closest to the Hector Mine epicentre, as noted above. Also, our model for seasonal de-



150 **Figure 3.** same as Figure 2 but for a far-field station.

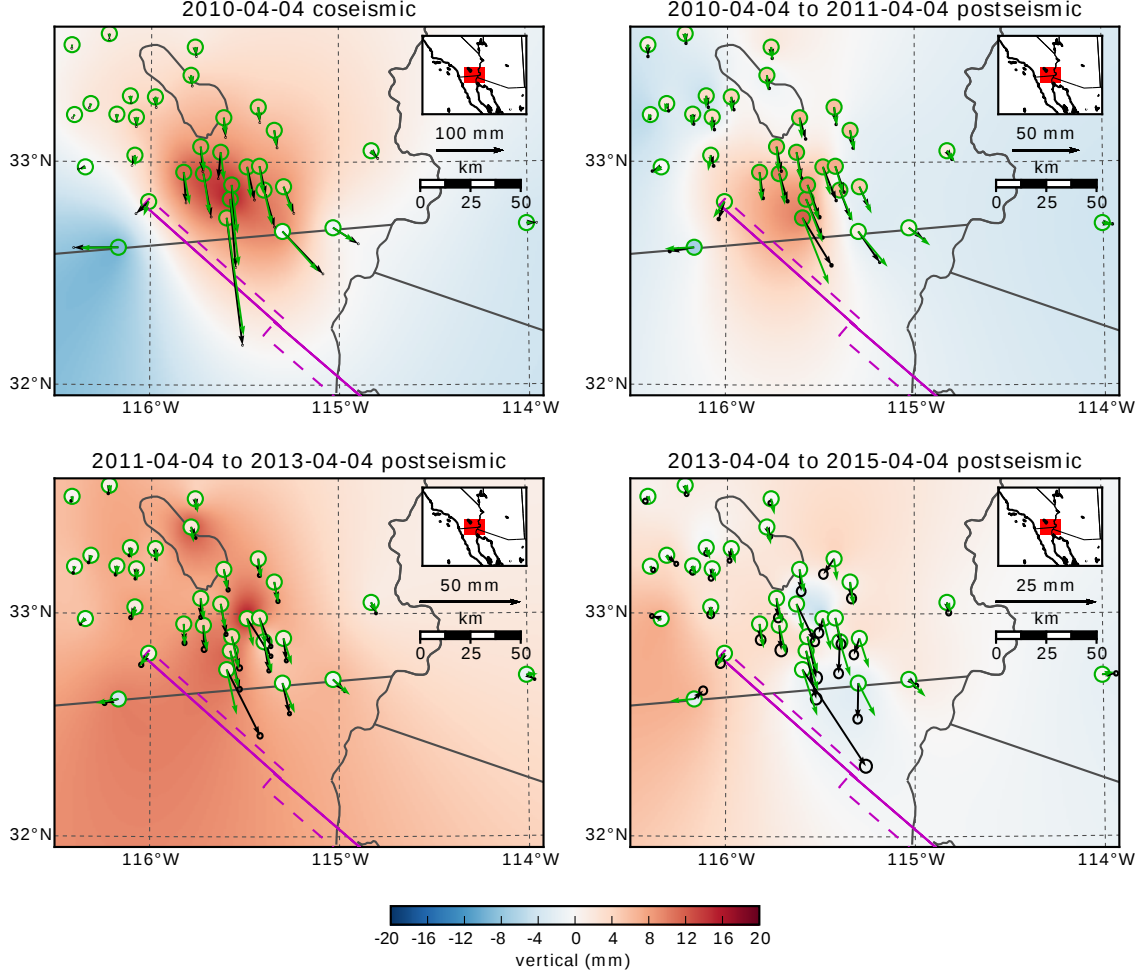
155 formation in eq. (2) assumes a constant amplitude over time, which means that any yearly vari-
 156 ability in the climatic conditions could introduce systematic residuals [Davis *et al.*, 2012]. In-
 157 deed, it would be more appropriate to consider the seasonal amplitudes $c_2 - c_5$ in eq. (2) as
 158 stochastic variables [Murray and Segall, 2005]. By using constant seasonal amplitudes, our es-
 159 timate of $u_{\text{post}}(t)$ seems to describe some of the unmodelled annual and semi-annual oscil-
 160 lations (e.g. Figure 3).

161 We show in Figures 4 and 5 the near and far-field postseismic displacements accumu-
 162 lated over the time intervals 0-1 years, 1-3 years, and 3-5 years, as well as the coseismic dis-
 163 placements. Stations at epicentral distances beyond ~ 200 km have an elevated rate of defor-
 164 mation for the first three years following the earthquake. This far-field deformation has a south-
 165 ward trend along the direction of the El Mayor-Cucapah P axis and a similar eastward trend
 166 can be seen in the few far-field stations in Arizona, located along the T axis. After three years,
 167 the trend in far-field postseismic deformation is barely perceptible. Most far-field stations dis-
 168 play an initial subsidence for the first year after the El Mayor-Cucapah earthquake followed
 169 by continued uplift. This trend in vertical deformation can be observed in all three of the quad-
 170 rats where postseismic data is available, which means that the vertical deformation does not
 171 exhibit an anti-symmetric quadrant pattern, as would be expected for postseismic processes.
 172 Although we use vertical deformation in our analysis in Section 3, we do not put an empha-
 173 sis on trying to describe the vertical deformation as it likely does not have postseismic ori-
 174 gins.

181 The near-field postseismic deformation is notably sustained when compared to the far-
 182 field deformation. Namely, the station in this study which is closest to the El Mayor-Cucapah
 183 epicentre, P496, has been moving at a steady rate of ~ 1.5 cm/yr to the south since about one
 184 year after the El Mayor-Cucapah earthquake. Vertical postseismic deformation in the near-field
 185 does display a quadrant pattern which is consistent with the coseismic vertical deformation,
 186 suggesting that it is resulting from postseismic processes. However, the vertical postseismic
 187 signal is only apparent for the first year after the earthquake (Figure 4). As with the far-field
 188 deformation, there is a general trend of uplift in the near-field after about one year.

189 **3 Postseismic Modeling**

193 We seek to find the mechanisms driving five years of postseismic deformation follow-
 194 ing the El Mayor-Cucapah earthquake and we consider afterslip and viscoelastic relaxation as
 195 candidate mechanisms. Poroelastic rebound has also been used to model postseismic defor-
 196 mation [e.g. Jónsson *et al.*, 2003]; however, Gonzalez-Ortega *et al.* [2014] found that poroe-



175 **Figure 4.** Near-field coseismic and cumulative postseismic displacements over the indicated time periods
 176 (black) as well as predicted displacements for our preferred model from Section 3.3 (green). Observed vertical
 177 deformation is shown as an interpolated field and predicted vertical displacements are shown within the
 178 circles at the base of each vector. Note that the interpolant is not well constrained in Mexico where there is no
 179 data available.

depth (km)	λ (GPa)	μ (GPa)	η_{eff} (10^{18} Pa s)	μ_k/μ
0-5	24.0	24.0	-	-
5-15	35.0	35.0	-	-
15-30	42.0	42.0	44.3	0.0
30-60	61.0	61.0	5.91	0.375
60-90	61.0	61.0	1.99	0.375
90-120	61.0	61.0	1.31	0.375
120-150	61.0	61.0	1.10	0.375
150- ∞	61.0	61.0	1.07	0.375

190 **Table 1.** Assumed and estimated material properties. λ and μ are assumed known *a priori* and are based on
 191 the values used for the coseismic model by Wei *et al.* [2011b]. The values for η_{eff} are estimated in Section 3.2
 192 and $\frac{\mu_k}{\mu}$ are the optimal shear moduli ratios found in Section 3.3 for a Zener rheology upper mantle.

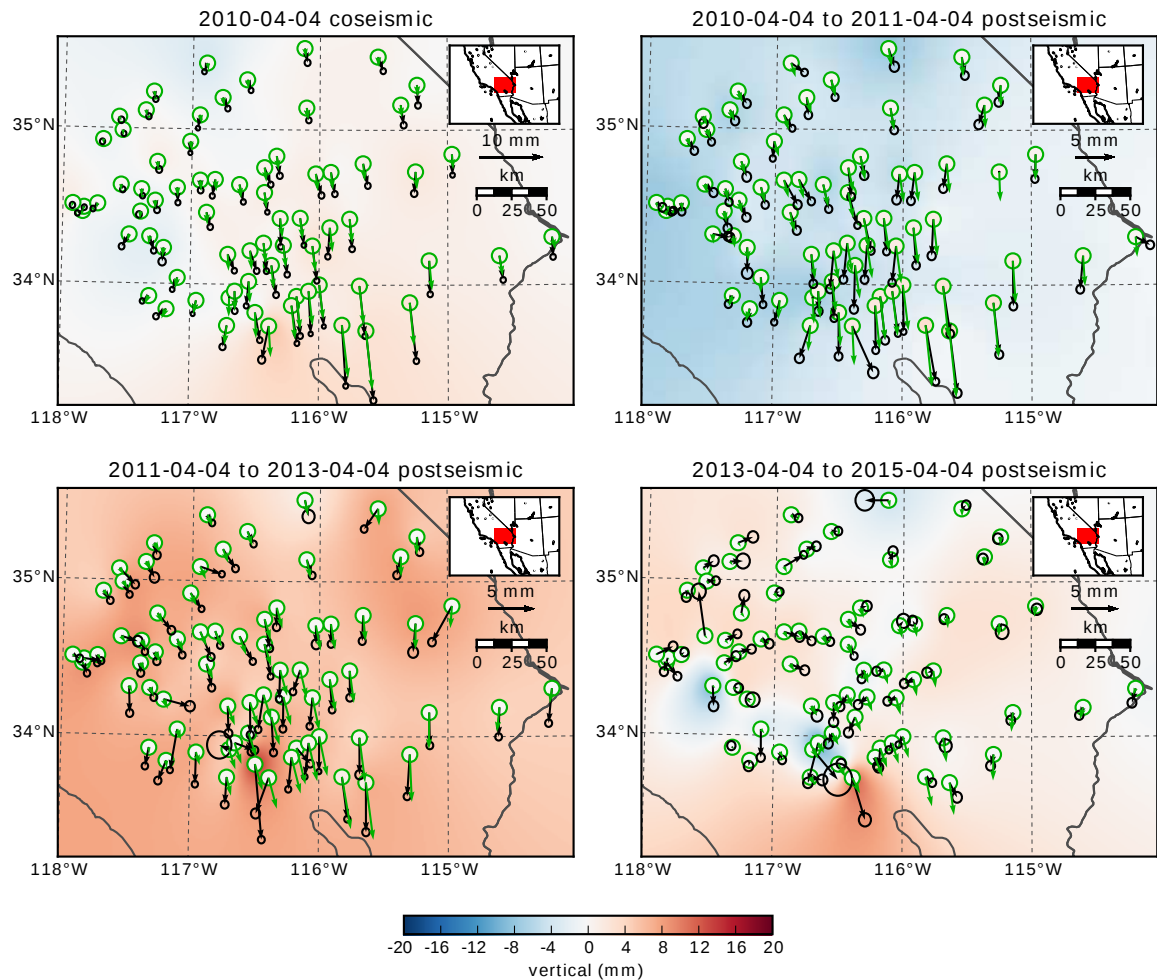


Figure 5. Same as Figure 4 but for far-field stations.

180

lastic rebound is unlikely to be a significant contributor to postseismic deformation following the El Mayor-Cucapah earthquake. Furthermore, we consider stations which are sufficiently far away from the main rupture that poroelastic rebound should be insignificant.

We estimate coseismic and time-dependent postseismic fault slip, both of which are assumed to occur on a fault geometry modified from *Wei et al.* [2011b]. Field studies [*Fletcher et al.*, 2014] and LIDAR observations [*Oskin et al.*, 2012] have revealed a significantly more complicated fault geometry than what was inferred by *Wei et al.* [2011b], especially within the Sierra Cucapah. However, we find that a relatively simple coseismic fault geometry based on [*Wei et al.*, 2011b] is adequate because most of the stations used in this study are sufficiently far from the El Mayor-Cucapah rupture zone that they are insensitive to the details in the fault geometry found by *Fletcher et al.* [2014] and *Oskin et al.* [2012]. The fault geometry used in this study (Figure 1) consists of the two main fault segments inferred by *Wei et al.* [2011b], where the northern segment runs through the Sierra Cucapah up to the US-Mexico border and the southern segment is the Indiviso fault which extends down to the Gulf of California. Both segments extend from the surface to 15 km depth. We extend the northern segment by 40 km to the north-west, motivated by the clustering of aftershocks on the northern tip of the coseismic rupture zone [*Hauksson et al.*, 2011; *Kroll et al.*, 2013]. This extended fault segment was also found to be necessary by *Rollins et al.* [2015] and *Pollitz et al.* [2012] in order to describe the postseismic deformation.

3.1 elastic inversion

We consider a variety of rheologic models for the lower crust and upper mantle. The simplest rheologic model is to consider them to be effectively elastic and isotropic. In such case, the rheologic parameters consist of the Lamé parameters, λ and μ , which are reasonably well known and we use the same values used by *Wei et al.* [2011b] throughout this paper (Table 3). The only unknown is the distribution of fault slip, which can be easily estimated from postseismic deformation through linear least squares. Using a subset of the GPS stations considered in this study, *Rollins et al.* [2015] found that three years of postseismic deformation following the El Mayor-Cucapah earthquake can be explained with afterslip on the coseismic fault plane without requiring any viscoelastic relaxation. We also perform an elastic slip inversion, but we use GPS stations within a larger radius about the El Mayor-Cucapah epicentre (400 km instead of \sim 200 km). Our forward problem describing predicted postseismic deformation u_{pred} in terms of time dependent fault slip, s , is

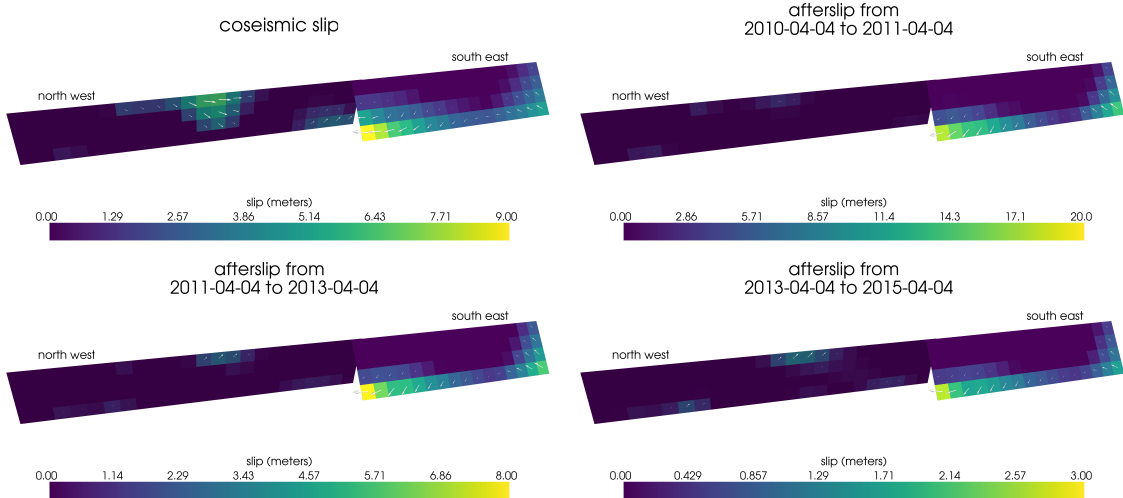
$$u_{\text{pred}}(x, t) = \int_F s(\xi, t) g(x, \xi) d\xi, \quad (9)$$

where F denotes the fault and $g(x, \xi)$ is the elastic Green's function describing displacement at surface position x resulting from slip at ξ on the fault. We estimate coseismic slip and the rate of afterslip at the discrete time intervals, 0.0-0.125, 0.125-0.25, 0.5-1.0, 1.0-2.0, 2.0-3.0, 3.0-4.0, and 4.0-5.0 years after the earthquake. Each fault segment is discretized into roughly 4 km by 4 km patches and we estimate a strike-slip and thrust component of slip for each patch. We impose that the direction of slip and slip rate are within 45° of right-lateral. We also add zeroth-order Tikhonov regularization so that our solution for s satisfies

$$\min_s \left(\left\| \frac{u_{\text{pred}}(s) - u_{\text{post}}}{\sigma_{\text{post}}} \right\|_2^2 + \lambda_s \|s\|_2^2 \right), \quad (10)$$

where σ_{post} is the uncertainty on postseismic displacements and λ_s is a penalty parameter which is chosen with a trade-off curve. We use Pylith [*Aagaard et al.*, 2013] to compute the Green's functions for this inversion as well as for the remaining inversions in this paper.

Our coseismic slip and afterslip solutions are shown in Figure 6. As with *Rollins et al.* [2015], we find that a large amount of afterslip on the southern fault segment is required to explain the observations. The potency of our inferred coseismic slip is $3.2 \times 10^9 \text{ m}^3$, equivalent to a Mw7.28 earthquake when assuming a shear modulus of 32 GPa. The potency of our



236 **Figure 6.** Coseismic slip and cumulative afterslip over the indicated intervals for the elastic model from
237 Section 3.1. Color indicates the magnitude of slip while arrows indicate the motion of the hanging wall.

224 inferred cumulative five years of afterslip is $6.1 \times 10^9 \text{ m}^3$, equivalent to a Mw7.46 earthquake,
225 which is unrealistically large if we consider afterslip to be driven by coseismically induced
226 stresses. Figure 7 shows the time series for the observed and predicted postseismic displace-
227 ments at stations along the El Mayor-Cucapah P axis. We show the radial component of dis-
228 placements with respect to the El Mayor-Cucapah epicentre and we also rescale the displace-
229 ments so that the difference between the minimum and maximum observed displacements are
230 the same for each station. Our elastic slip model accurately describes near-field postseismic
231 deformation and systematically underestimates postseismic deformation at epicentral distances
232 $\gtrsim 150 \text{ km}$. When the fault segments used in the inversion are extended down to 30 km depth,
233 rather than 15 km, the systematic far-field residuals are smaller but remain apparent. Because
234 an elastic model requires an unrealistic amount of afterslip and is unable to predict far-field
235 deformation, we move on to consider viscoelastic models in the next section.

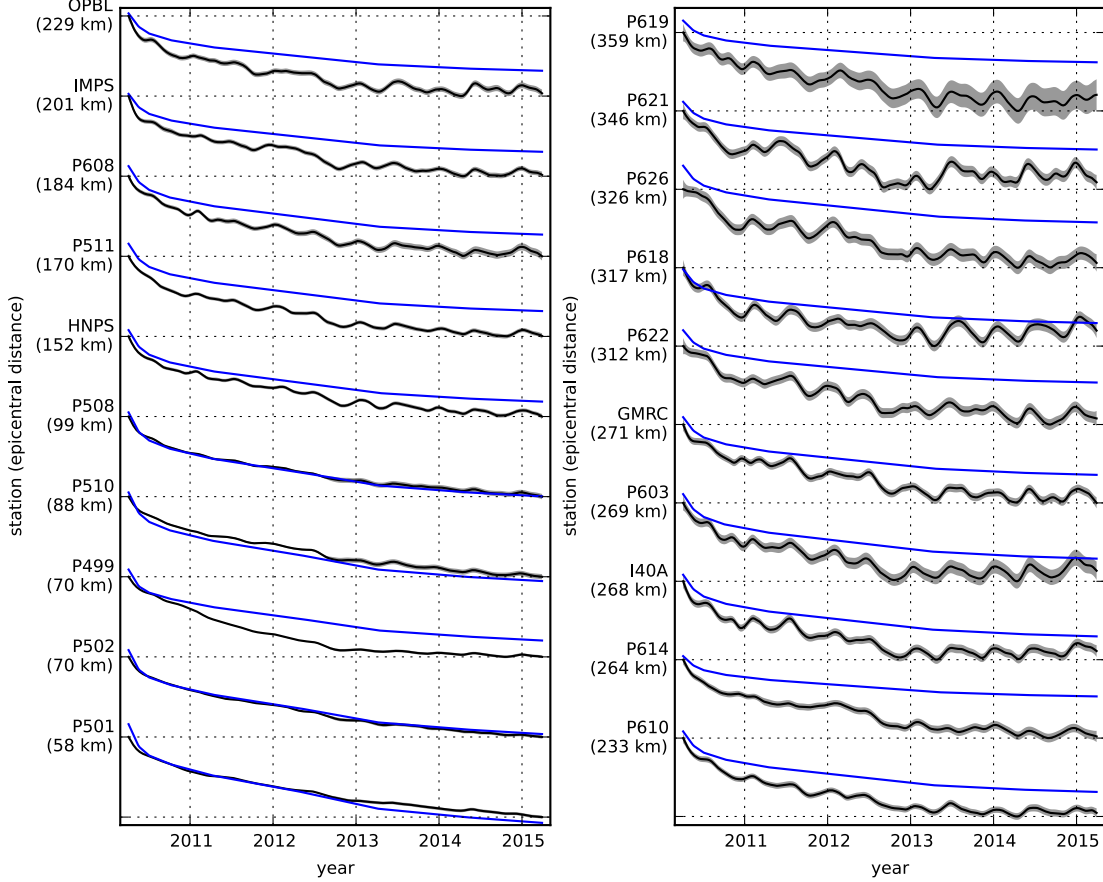
243 3.2 constraints on effective viscosity

244 For any linear viscoelastic rheology of the crust and mantle, postseismic displacements
245 resulting from time dependent fault slip can be described as

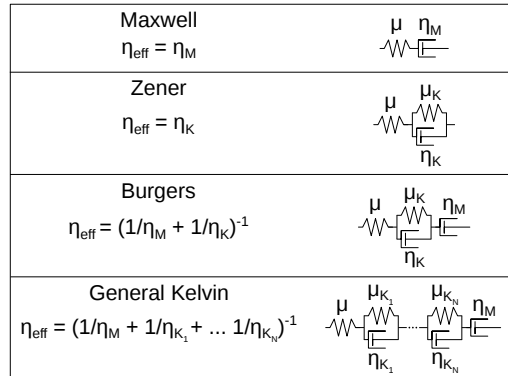
$$246 u_{\text{pred}}(x, t) = \int_F s(\xi, t) g(x, \xi) d\xi + \int_0^t \int_F s(\xi, \tau) f(t - \tau, x, \xi) d\xi d\tau \quad (11)$$

247 where $f(t, x, \xi)$ describes the time-dependent velocity at x resulting from viscoelastic relax-
248 ation of stresses induced by slip at ξ . f is a function of λ , μ , and any additional rheologic pa-
rameters controlling the viscoelastic response, which are generally not well known. Schematic
representations of the viscoelastic rheologic models considered in this study are shown in Fig-
ure 8. We discuss these rheologic models and their use in geophysical studies in Section 4.

249 In order to greatly simplify the inverse problem, we use the method described in *Hines*
250 and *Hetland* [2016] to constrain an initial effective lithospheric viscosity structure from the
251 early postseismic deformation. Our method utilizes the fact that coseismic stresses through-
252 out the crust and upper mantle depend on the instantaneous elastic parameters and are inde-
253 pendent of the viscoelastic parameters which we wish to estimate. Immediately following an
254 earthquake, each parcel will have a strain rate that is proportional to the coseismic stress and
255 inversely proportional to the parcel's effective viscosity, η_{eff} . Using one-dimensional viscoelas-



238 **Figure 7.** Scaled radial component of observed postseismic displacements u_{obs} (black) and displacements
 239 predicted by the best fitting elastic model u_{pred} (blue). Downward motion indicates that the station is moving
 240 toward the El Mayor-Cucapah epicentre. Displacement time series are scaled so that the minimum and max-
 241 imum observed values lie on the grid lines. The 68% confidence interval for the observed displacements are
 242 shown in gray.



249 **Figure 8.** Schematic illustration of rheologic models considered in this paper as well as their effective
 250 viscosities.

tic models, we define the effective viscosity as

$$\eta_{\text{eff}} = \left. \frac{\sigma}{\dot{\varepsilon}} \right|_{t=0} \quad (12)$$

where σ is an applied stress at $t = 0$ and $\dot{\varepsilon}$ is the resulting strain rate. Figure 8 shows how η_{eff} relates to the parameters for various linear viscoelastic rheologies. We can deduce that the initial rate of surface deformation resulting from viscoelastic relaxation is a summation of the surface deformation resulting from relaxation in each parcel, scaled by the reciprocal of the parcel's effective viscosity. That is to say

$$f(0, x, \xi) = \int_L \frac{h(x, \xi, \zeta)}{\eta_{\text{eff}}(\zeta)} d\zeta, \quad (13)$$

where L denotes the crust and mantle and $h(x, \xi, \zeta)$ describes the initial rate of deformation resulting from viscoelastic relaxation at ζ induced by slip at ξ . We can combine eq. (13) with eq. (11) to get a first order approximation for early postseismic deformation,

$$u_{\text{pred}}(x, t) \approx \int_F s(\xi, t) g(x, \xi) d\xi + \int_0^t \int_F \int_L \frac{s(\tau, \xi)}{\eta_{\text{eff}}(\zeta)} h(x, \xi, \zeta) d\xi d\zeta d\tau, \quad (14)$$

which is valid for as long as the rate of deformation resulting from viscoelastic relaxation is approximately constant.

Details on how eq. (14) is used to estimate s and η_{eff} from postseismic deformation can be found in *Hines and Hetland* [2016]. A non-linear Kalman filter based inverse method can also be used to estimate s and η_{eff} in a manner akin to *Segall and Mathews* [1997] or *McGuire and Segall* [2003], in which we would not have to explicitly impose a time dependent parametrization of s . We have thoroughly explored Kalman filter based approaches, but we ultimately prefer the method described in *Hines and Hetland* [2016] because of its relative simplicity. Moreover, we believe the piecewise continuous representation of slip with respect to time to be sufficiently general for the resolving power of these GPS data.

Although eq. (14) may only be valid for a short portion of the postseismic period, its utility becomes apparent when noting that g and h are only functions of the fault geometry and instantaneous elastic properties, λ and μ , and thus g and h can be computed numerically as a preprocessing step. The forward problem in eq. (14) can be rapidly evaluated for any realization of s and η_{eff} . This is in contrast to evaluating the full forward problem, eq. (11), numerically for each realization of s and unknown rheologic properties.

We perform an initial inversion of postseismic displacements using the approximation in eq. (14). We estimate coseismic slip and afterslip with the same spatial and temporal discretization as in Section 3.1. Simultaneously, we estimate η_{eff} within six vertically stratified layers which have depths ranging from 15-30 km, 30-60 km, 60-90 km, 90-120 km, 120-150 km, as well as from 150 km to the bottom of our numerical model domain at 800 km. We again restrict fault slip to occur between 0 and 15 km depth, which is done in order to help eliminate inevitable non-uniqueness in the inversion. It has long been recognized that fault slip at sufficiently great depths can produce surface deformation that is indistinguishable from viscoelastic relaxation, at least in two-dimensional earthquake models [*Savage*, 1990]. Additionally, we note that when simultaneously estimating both afterslip and viscosity in the lower crust, the inverse problem becomes particularly ill-posed. This ill-posedness is illustrated in Figure 9, which shows the displacements resulting from a meter of slip on a fault extending from 15 to 30 km depth and the initial velocity resulting from subsequent viscoelastic relaxation in the lower crust, which is given a viscosity of 10^{18} Pa s. In this demonstration, the viscoelastic relaxation is entirely driven by the fault slip in the lower crust. The horizontal displacements from fault slip are in the opposite direction as the displacements resulting from viscoelastic relaxation. This means that surface displacements resulting from afterslip at lower crustal depths can be cancelled out, at least partially, by a low viscosity lower crust. We eliminate this null space by allowing only one mechanism in the lower crust, which we choose to be viscoelastic relaxation. This is not to say that we do not believe deep afterslip to be a possibility; rather,

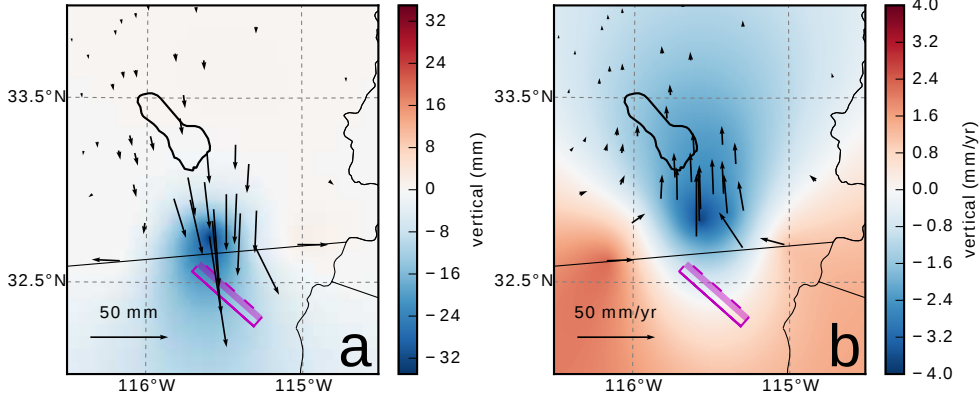


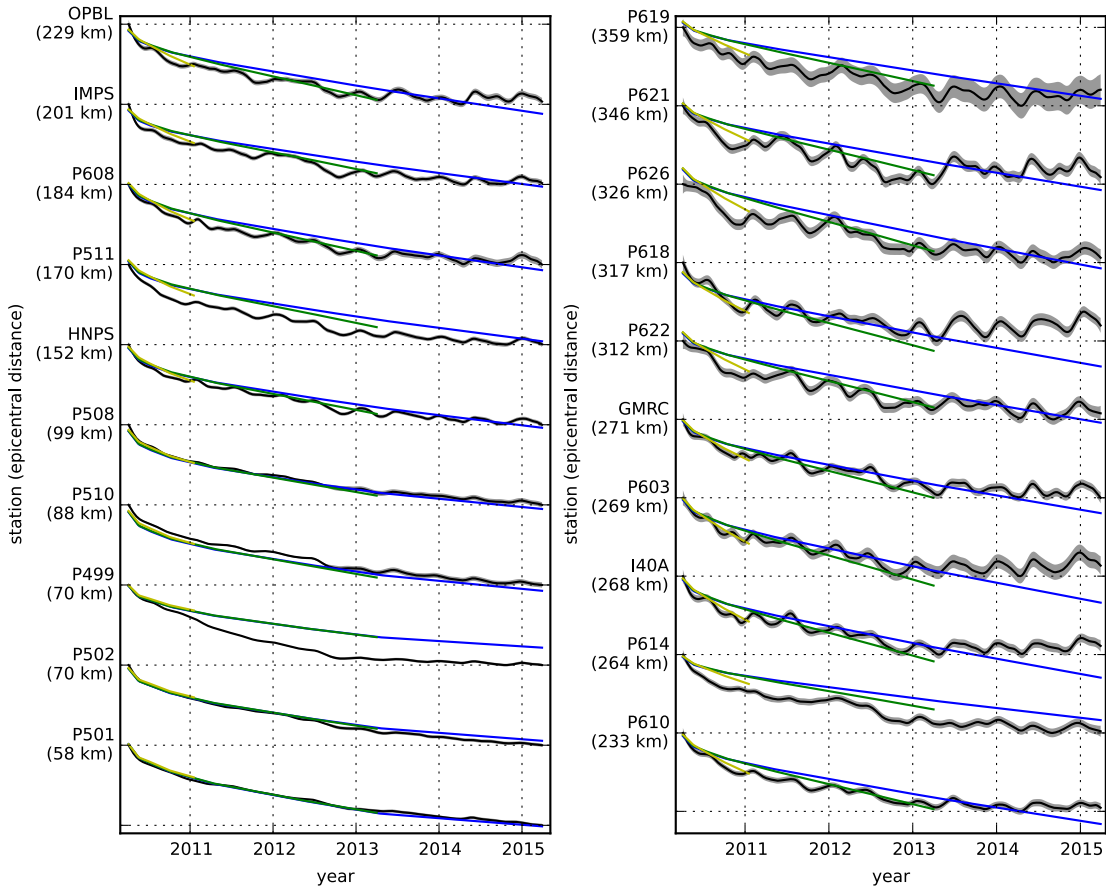
Figure 9. Displacements resulting from fault slip at lower crustal depths (a), and initial velocities resulting from subsequent relaxation of a viscoelastic lower crust (b). The fault segment dips 75° to the north-east and its surface projection is outlined in magenta. The highlighted area on the fault extends from 15 to 30 km depth and indicates where 1 meter of right-lateral slip was imposed. The elastic properties of the crust and mantle are the same as in Table 3 and $\eta_{\text{eff}} = 10^{18}$ Pa s in the lower crust. Vertical displacements are interpolated between station locations.

we restrict slip to seismogenic depths as a modelling necessity. Although, it has been noted that the pattern of vertical postseismic deformation following the El Mayor-Cucapah earthquake indicates that a significant amount of afterslip must be shallow [Rollins *et al.*, 2015].

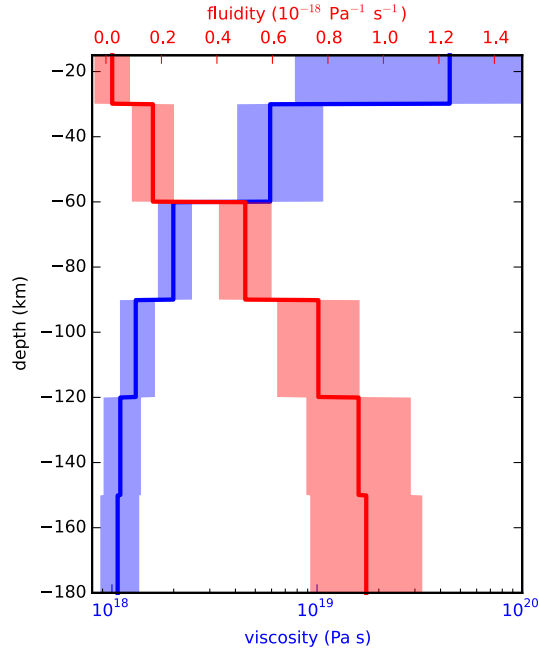
We must determine at which point the early postseismic approximation breaks down, which we will denote as t_{bd} . As noted, eq. (14) is valid for approximately as long as the rate of deformation resulting from viscoelastic relaxation is approximately constant. We can almost certainly assume that deformation at the most far-field stations, which are ~ 400 km away from the El Mayor-Cucapah epicentre, is the result of viscoelastic relaxation. The approximation should then be valid for as long as a linear trend adequately approximates the far-field deformation. Using this logic, it would appear that t_{bd} is about one year after the El Mayor-Cucapah earthquake. Another way to determine t_{bd} is to find the best fitting prediction of eq. (14) to observed deformation using increasing durations of the postseismic time series. t_{bd} should be the point when eq. (14) is no longer capable of describing the observed deformation without incurring systematic misfits. When using eq. (14) to fit the entire five years of postseismic displacements, we see that the near-field displacements (e.g., station P501) are accurately predicted but when looking at displacement in the far-field (e.g., station P621) we see that eq. (14) overestimates the rate of deformation in the later postseismic period and underestimates the rate of deformation in the early period (Figure 10). Due to the low signal-to-noise ratios for far-field stations, it is difficult to determine at what point eq. (14) is no longer able to predict the observed displacements without incurring any significant systematic misfit; however, we settle on $t_{\text{bd}} = 0.8$ years after the earthquake, while acknowledging that the choice is subjective. As noted in Hines and Hetland [2016], overestimating t_{bd} will result in a bias towards overestimating η_{eff} , while picking a t_{bd} which is too low will not necessarily result in a biased estimate of η_{eff} , although the uncertainties would be larger. We can then consider inferences of η_{eff} to be an upper bound on the viscosity needed to describe the far-field rate of deformation during the first 0.8 years of postseismic deformation.

We estimate coseismic slip, afterslip, and effective viscosity by solving

$$\min_{s, \eta_{\text{eff}}} \left(\left\| \frac{u_{\text{pred}}(s, \eta_{\text{eff}}) - u_{\text{post}}}{\sigma_{\text{post}}} \right\|_2^2 + \lambda_s \|s\|_2^2 + \lambda_\eta \|\nabla \eta_{\text{eff}}^{-1}\|_2^2 \right), \quad (15)$$



319 **Figure 10.** Observed postseismic displacements (black) and best fitting predictions of eq. (14) to 5.0 (blue),
 320 3.0 (green), and 0.8 (yellow) years of the postseismic data.

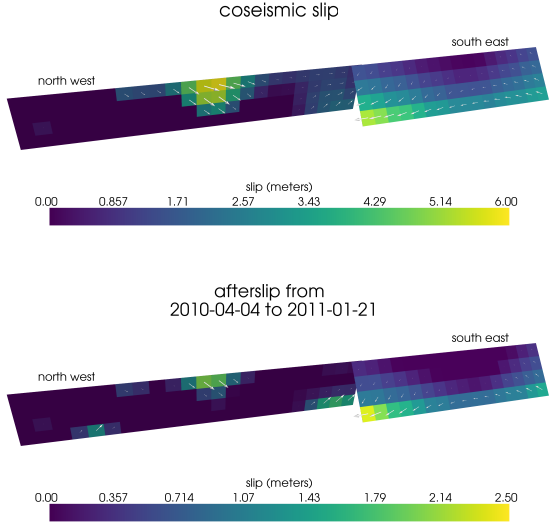


345 **Figure 11.** Effective viscosities and associated fluidities inferred by fitting eq. (14) to the first 0.8 years of
 346 postseismic displacements. 95% confidence intervals, estimated from bootstrapping, are indicated by color
 347 fields.

321 where u_{post} consists of the first 0.8 years of postseismic deformation and u_{pred} are the pre-
 322 dicted displacements from eq. (14). Due to inherent non-uniqueness, we have added zeroth-
 323 order Tikhonov regularization to estimates of s , and second-order Tikhonov regularization to
 324 estimates of effective fluidity, η_{eff}^{-1} . The degree to which we impose the regularization on slip
 325 and fluidity is controlled by the penalty parameters λ_s and λ_η , which are chosen with trade-
 326 off curves. Our goal here is to get a prior constraint on η_{eff} to minimize the amount of search-
 327 ing we have to do when describing the postseismic deformation over the full five years, which
 328 we do in Section 3.3. Estimates of s made here will not be used in Section 3.3, and so the
 329 motivation behind adding regularization to s is to ensure that the slip driving viscoelastic re-
 330 laxation in eq. (14) is sensible.

331 Our inferred estimates of effective viscosities, and corresponding fluidities, are shown
 332 in Figure 11. Although fluidity is rarely used in geophysical literature, eq. (13) is linear with
 333 respect to fluidity and so the fluidity indicates the amplitude of the viscoelastic signal com-
 334 ing from each layer. We also show the 95% confidence intervals for estimated viscosities and
 335 fluidities but we note that the uncertainties tend to be underestimated due to the added reg-
 336 ularization [Aster *et al.*, 2011]. A robust feature that we see is that the largest jump in fluid-
 337 ity is at 60 km depth, which is consistent with the range of lithosphere-asthenosphere bound-
 338 ary depths inferred by Lekic *et al.* [2011]. This transitional depth is also consistent with the
 339 the viscosity structure required to explain far-field postseismic deformation following the Hec-
 340 tor Mine earthquake [Freed *et al.*, 2007]. We find that the viscosity below 60 km depth needs
 341 to be $\sim 1 \times 10^{18}$ Pa s to describe the early rate of postseismic deformation at far-field stations
 342 while the lower crust and uppermost mantle need to be relatively stronger. The viscosity of
 343 the lower crust is the least well constrained as there is no evidence of relaxation in that layer,
 344 meaning that it is effectively elastic over the first 0.8 years after the earthquake.

348 Our initial estimate for coseismic slip and cumulative afterslip over the first 0.8 years
 349 after the El Mayor-Cucapah earthquake are shown in Figure 12. Similar to our elastic slip model
 350 from Section 3.1, a significant amount of right-lateral and normal coseismic slip is inferred



365 **Figure 12.** Coseismic slip and afterslip inferred by fitting eq. (14) to the first 0.8 years of postseismic
366 displacements.

351 to be on the Sierra Cucapah fault segment and in a region that is consistent with field studies [Fletcher *et al.*, 2014] and the coseismic slip from Wei *et al.* [2011b]. The potency of inferred coseismic slip is $3.3 \times 10^9 \text{ m}^3$, which is also about the same as that inferred from Section 3.1. The present inference of afterslip on the Indiviso fault is significantly less than what was found in the Section 3.1 where we did not account for viscoelasticity. When fault slip is simultaneously estimated with a lithospheric and asthenospheric viscosity, the potency of inferred afterslip over the first 0.8 years after the earthquake is $0.85 \times 10^9 \text{ m}^3$, compared to $3.46 \times 10^9 \text{ m}^3$ when we assume crust and upper mantle are elastic. The significant amount of afterslip inferred on the Indiviso fault seems to be compensating for unmodelled viscoelastic relaxation at depths greater than 60 km. The fact that there is still an appreciable amount of afterslip inferred on the Indiviso fault even when allowing for viscoelastic relaxation in the lower crust and upper mantle raises the question of whether it is compensating for viscoelastic relaxation that is more localized than what we allow for since we only estimate depth dependent variations in viscosity.

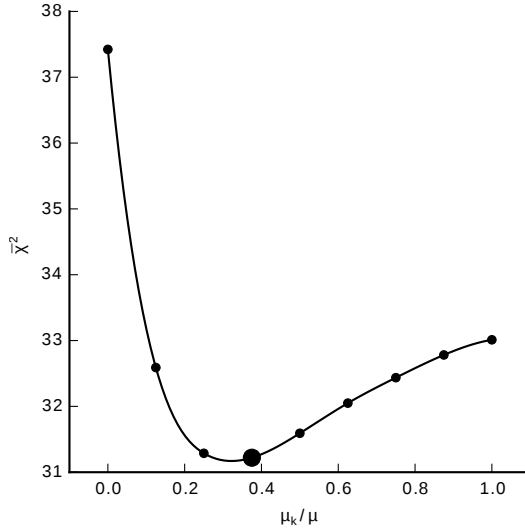
367 3.3 Full Inversion

In the previous section, we used the inverse method from Hines and Hetland [2016] to constrain the effective viscosity structure required to explain the first 0.8 years of postseismic deformation. In this section, we use these effective viscosities as a prior constraint when searching for models which are capable of describing the available five years of postseismic data, where our forward problem is now eq. (11) rather than the approximation given by eq. (14). We perform a series of coseismic slip and afterslip inversion assuming a variety of rheologies for the lower crust and upper mantle which are consistent with our findings from Section 3.2. We appraise each model using the mean chi-squared value,

$$\bar{\chi}^2 = \frac{1}{N} \left\| \frac{u_{\text{pred}} - u_{\text{obs}}}{\sigma_{\text{obs}}} \right\|_2^2, \quad (16)$$

368 where N is the number of observations.

369 We first assume that the crust and mantle can be described with a Maxwell rheology,
370 and we set η_M equal to our inference of η_{eff} . We compute f and g from eq. (11) using the

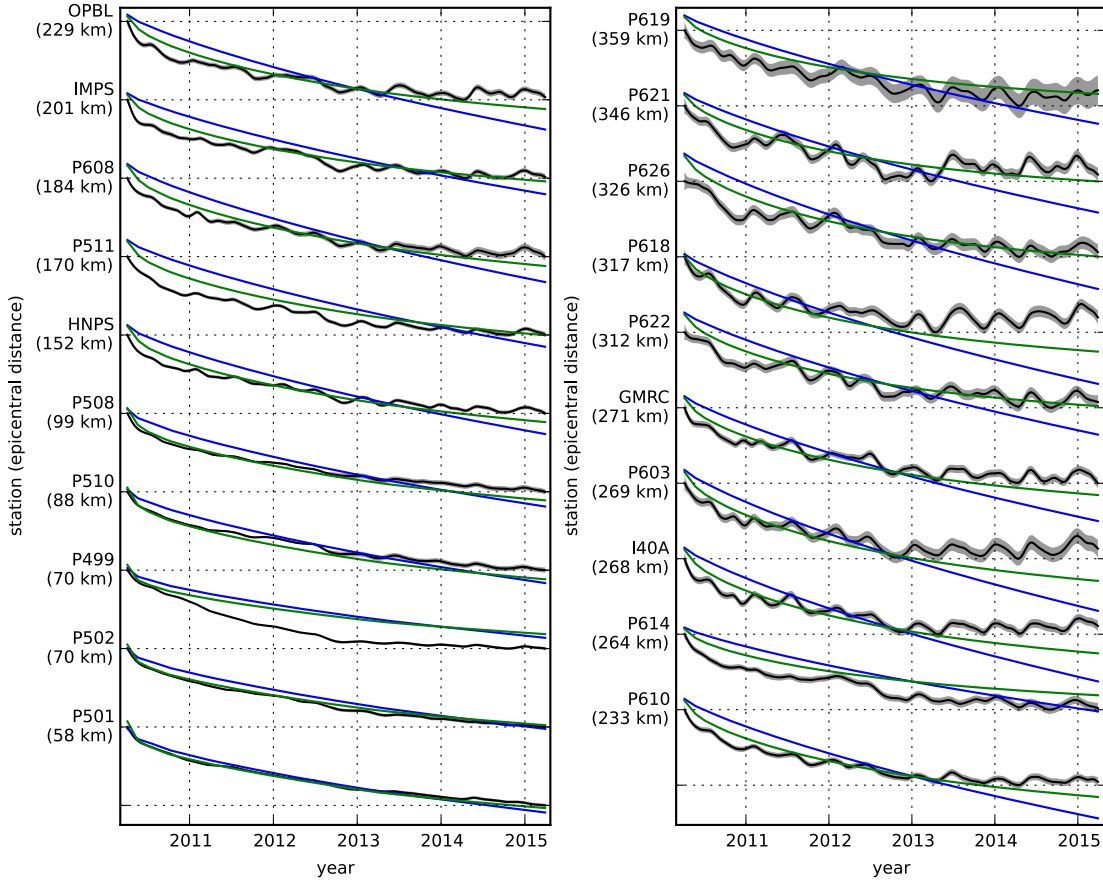


398 **Figure 13.** Mean chi-squared value for the best fitting slip model as a function of the transient shear modu-
 399 lus relative to the elastic shear modulus in a Zenner upper mantle. Large dot indicates our preferred ratio.

371 finite element software, Pylith [?], and assume the same spatial and temporal discretization
 372 of s as in Sections 3.1 and 3.2. We estimate s using linear least squares and we find $\bar{\chi}^2 =$
 373 37.4. For comparison, $\bar{\chi}^2 = 35.3$ for the elastic model from Section 3.1. The Maxwell vis-
 374 coelastic model has a larger misfit because it tends to overestimate the rate of deformation af-
 375 ter about three years (Figure 14). Since our initial estimates of η_{eff} may be biased towards over-
 376 estimating viscosities, we have also performed the slip inversion where we use uniformly lower
 377 viscosities in the crust and mantle. However, decreasing the viscosity only increases the mis-
 378 fit. Although, the viscosities used here are consistent with the successful Maxwell viscoelas-
 379 tic models found by *Rollins et al.* [2015] and *Spinler et al.* [2015], which had mantle viscosi-
 380 ties on the order of 10^{18} Pa s, we find that such a model is incapable of describing the en-
 381 tire postseismic time series. *Pollitz et al.* [2001] similarly recognized this deficiency in a Maxwell
 382 rheology, which then motivated their exploration of a Burgers rheology upper mantle [*Pollitz*,
 383 2003].

384 Rather than exploring a Burgers rheology mantle, which introduces two new parame-
 385 ters that need to be estimated, η_K and μ_K , we first consider a Zener rheology for the man-
 386 tle, which only introduces one additional unknown parameter, μ_K . We assume that the lower
 387 crust still has a Maxwell rheology. The steady-state viscosity, η_M , in the crust and the tran-
 388 sent viscosity, η_K , in the mantle are set equal to the inferred effective viscosities. We then
 389 estimate the ratio of shear moduli, $\frac{\mu_K}{\mu}$. We compute nine different sets of Green's functions,
 390 f and g , using Pylith, where we assume values of $\frac{\mu_K}{\mu}$ ranging from 0 to 1. The former be-
 391 ing a degenerate case where the Zener model reduces to the above Maxwell model. We es-
 392 timate coseismic slip and afterslip for each realization of $\frac{\mu_K}{\mu}$. The shear moduli ratio that yields
 393 to best prediction to the observed postseismic displacements is found to be 0.375 with a mis-
 394 fit of $\bar{\chi}^2 = 31.2$ (Figure 13). The improvement in the Zener model over the Maxwell model
 395 can be clearly seen in the fit to the far-field data (Figure 14). The Zener model does a signif-
 396 icantly better job at explaining the transient rate of far-field deformation throughout the five
 397 years.

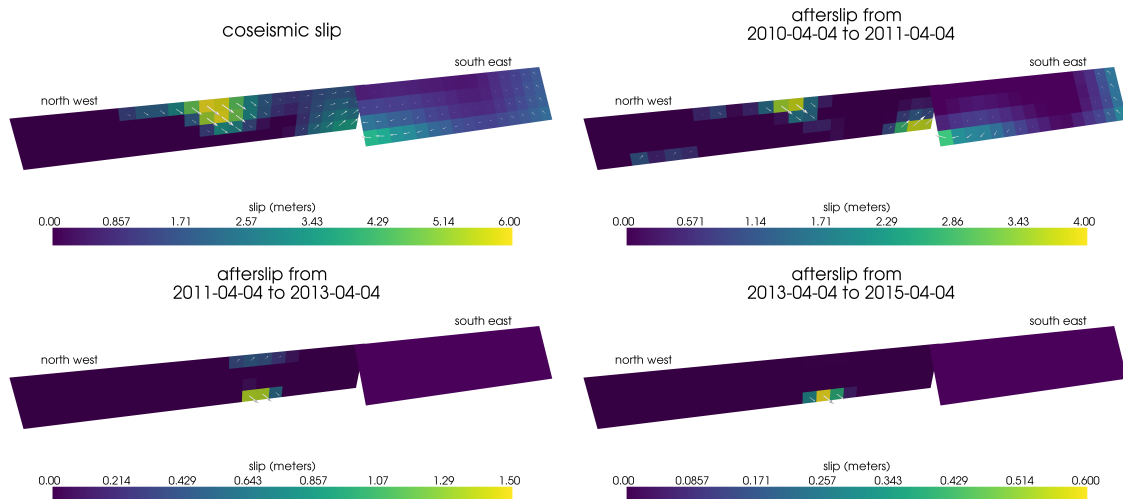
403 Because we are able to adequately describe the available five years of postseismic de-
 404 formation with a Zener model, we do not find it necessary to explore the parameter space for
 405 a more complicated Burgers rheology. However, since the Zener model is a Burgers model with
 406 an infinite steady-state viscosity, we can conclude that any Burgers rheology that has a tran-



400 **Figure 14.** Observed postseismic displacements (black) and predicted postseismic displacements for the
 401 best fitting slip models when using a Maxwell (blue) and Zener (green) rheology in the upper mantle. The
 402 effective viscosities are the same for both models and are shown in Figure 11.

407 transient viscosity consistent with that found in Section 3.2 and a steady-state viscosity of $\gtrsim 10^{20}$
 408 Pa s, which is effectively infinite on the time scale of five years, would also be able to sat-
 409 isfactorily describe the observable postseismic deformation.

410 The regularized inference of coseismic slip and afterslip for our preferred Zener model
 411 is shown in Figure 15, and the predicted postseismic displacements are shown Figures 4, 5 and
 412 14. Overall, the trends in the near-field and far-field transient deformation are accurately de-
 413 scribed by our preferred model. In particular, the trends in far-field deformation are much bet-
 414 ter described by our preferred Zener model than either an elastic model or a model with a Maxwell
 415 viscoelastic mantle (Figure 14). There are a few areas where we have notable misfit. Most of
 416 our misfit is for the near-field stations in the Imperial Valley, and we attribute this misfit to
 417 our relatively simple fault geometry, which does not account for potential fault slip in the Im-
 418 perial Valley triggered by the El Mayor-Cucapah earthquake [Wei *et al.*, 2011a, 2015]. In par-
 419 ticular, we are unable to model the sustained, rapid rate of deformation at station P496, which
 420 suggests that this station could be influenced by a more localized deformation mechanism than
 421 is considered in this study. Additionally, we see systematic misfit in the later postseismic pe-
 422 riod west of the Landers and Hector Mine earthquakes, which may be the result of unmod-
 423 elled postseismic deformation resulting from those earthquakes. Lastly, there are clear discrep-
 424 ancies between the observed and predicted vertical deformation following the first year after
 425 the El Mayor Cucapah earthquake. We observe a broad uplift throughout Southern Califor-
 426 nia, which is inconsistent with any postseismic model.



427 **Figure 15.** Inferred coseismic slip and afterslip when assuming a Maxwell rheology in the lower crust
 428 and a Zener rheology in the upper mantle. η_K in the mantle and η_M in the crust are set equal to the effective
 429 viscosities from Figure 11. We use $\frac{\mu_K}{\mu} = 0.375$ in the upper mantle.

430 The inferred coseismic potency is $3.0 \times 10^9 \text{ m}^3$, equivalent to a Mw7.26 earthquake,
 431 and the potency of five years of afterslip is $1.1 \times 10^9 \text{ m}^3$. Most of the afterslip in our pre-
 432 ferred model occurs within the first year after the earthquake with a significant amount inferred
 433 to be shallow and in the Sierra Cucapah. The afterslip within the first year is accounting for
 434 the most rapid near-field transient deformation. After 1 year, afterslip is inferred to be deeper
 435 down on the Sierra Cucapah segment, which is describing much of the sustained near-field post-
 436 seismic deformation. We emphasize, that the GPS station closest to our inferred afterslip, P496,
 437 is still about 30 km away, which is too far away for us to conclusively argue for sustained lo-
 438 calized deformation rather shallow distributed deformation. The deep afterslip inferred after
 439 1 year could potentially be describing deformation resulting from lower crustal flow. To test

440 this, we have modified our preferred model by decreasing the lower crustal viscosity from $5.91 \times$
 441 10^{19} Pa s to 1×10^{19} Pa s, which is still consistent with our viscosity inference from Sec-
 442 tion 3.2, and inverted for fault slip. We find that a model with a weaker lower crust adequately
 443 describes the postseismic displacements without any afterslip after 1 year, while still requir-
 444 ing about the same amount of afterslip over the first year. We do believe that the early shal-
 445 low afterslip on the Sierra Cucapah segment is a robust feature in our preferred model, while
 446 we are not confident in our inference of later deep afterslip.

447 4 Discussion

448 It has long been recognized that deep afterslip and viscoelastic relaxation following an
 449 upper crustal earthquake can result in similar horizontal ground deformation at the surface [e.g.
 450 *Savage*, 1990; *Pollitz et al.*, 2001; *Hearn*, 2003; *Feigl and Thatcher*, 2006]. The similarity of
 451 the horizontal postseismic deformation results in a non-uniqueness in inferences of afterslip
 452 or viscoelastic relaxation. In contrast, the spatial pattern of vertical postseismic deformation
 453 has been proposed to be a discriminant between deep afterslip and viscoelastic relaxation [e.g.
 454 *Pollitz et al.*, 2001; *Hearn*, 2003]. It is, however, important to note that patterns of vertical de-
 455 formation are very sensitive to the depth-dependence of viscosity below the upper crust [?*Het-*
 456 *land and Zhang*, 2014]. The similarity between deformation resulting from deep afterslip and
 457 viscoelastic relaxation of coseismic stresses is different from the ill-posedness described in Sec-
 458 tion 3.2. In our method, any inferred afterslip will also mechanically drive additional viscoelas-
 459 tic relaxation. The horizontal deformation resulting from deep afterslip will generally be in
 460 the opposite direction as horizontal deformation resulting from viscoelastic relaxation of sub-
 461 sequent stresses in the lower crust (Figure 9). As a result, there is a trade-off between infer-
 462 ences of deep afterslip and lower crustal viscosity. In our synthetic tests in ?, we have found
 463 that inverting surface deformation for afterslip and viscosity within the same depth interval
 464 tends to result in overestimated afterslip and an underestimated viscosity at that depth.

465 Most postseismic studies assume Maxwell viscoelasticity in the lower crust and upper
 466 mantle [e.g. *Nur and Mavko*, 1974; *Pollitz et al.*, 2000; *Hetland*, 2003; *Freed et al.*, 2006; *John-*
 467 *son et al.*, 2009; *Hearn et al.*, 2009], which is the simplest viscoelastic rheologic model. In South-
 468 ern California, postseismic studies following the Landers [*Pollitz et al.*, 2000], Hector Mine
 469 [*Pollitz et al.*, 2001], and El Mayor-Cucapah earthquake [*Spinler et al.*, 2015; *Rollins et al.*, 2015],
 470 have assumed Maxwell viscoelasticity in the lower crust and upper mantle and have inferred
 471 upper mantle viscosities on the order of 10^{17} to 10^{18} Pa s and lower crust viscosities $\gtrsim 10^{19}$
 472 Pa s. These postseismic studies are consistent with *Kaufmann and Amelung* [2000] and *Cava-*
 473 *alié et al.* [2007], who found that an upper mantle viscosity of 10^{18} Pa s and a crustal visc-
 474 osity $\gtrsim 10^{20}$ Pa s are necessary to describe subsidence resulting from changes in loading from
 475 Lake Mead. This isostatic adjustment is a process with similar spatial and temporal scales as
 476 postseismic deformation, and thus the inferred viscosities of these two types of studies would
 477 likely agree. While these studies found viscosities that are consistent with our effective vis-
 478 cosities from Section 3.2, they are inconsistent with viscosity estimates made from geophys-
 479 ical processes that occur over longer time scales. For example, *Lundgren et al.* [2009] found
 480 that lower crust and upper mantle viscosities on the order of 10^{21} and 10^{19} Pa s, respectively,
 481 are needed to describe interseismic deformation along the Southern San Andreas fault zone
 482 in the Salton Sea region. An even higher mantle viscosity, on the order of 10^{20} Pa s, is re-
 483 quired to describe isostatic adjustment resulting from the draining of Lake Bonneville, which
 484 occurs on the time scales of 10^4 years [*Crittenden*, 1967; *Bills and May*, 1987].

485 An additional deficiency with the Maxwell rheology is that it predicts a steady decay
 486 in the rate of postseismic deformation over time, which fails to describe the commonly ob-
 487 served rapid early transience followed by a relatively steady rate of postseismic deformation.
 488 One could explain the early transient postseismic deformation with fault creep and the later
 489 phase with relaxation in a Maxwell viscoelastic lower crust and upper mantle [e.g *Hearn et al.*,
 490 2009; *Johnson et al.*, 2009]. However, postseismic deformation at distances greater than ~ 200
 491 km from the El Mayor-Cucapah epicentre can only be attributed to viscoelastic relaxation [*Freed*

492 *et al.*, 2007] and we have demonstrated that the far-field deformation cannot be explained with
 493 a Maxwell rheology (Figure 14).

494 We found that a Zener rheology in the upper mantle with a transient viscosity of $\sim 10^{18}$
 495 Pa s does a noticeably better job at predicting far-field postseismic deformation. A general-
 496 ization of the Zener viscoelastic model, schematically represented as several Kelvin elements
 497 connected in series, is commonly used to describe seismic attenuation [Liu *et al.*, 1976]. The
 498 highest viscosity needed to describe seismic attenuation is on the order of 10^{16} Pa s [Yuen and
 499 Peltier, 1982] which has a characteristic relaxation time on the order of days. Even though
 500 our inferred transient viscosity is orders of magnitude larger than that required for seismic at-
 501 tenuation models, the two models are not incompatible. Rather, the delayed elasticity in seis-
 502 mic attenuation models occurs on such short time scales that it can be considered part of the
 503 instantaneous elastic phase of deformation associated with the preferred Zener model in this
 504 study.

505 Of course, it has long been recognized that a Zener rheology provides an incomplete de-
 506 scriptions of the asthenosphere, as it does not have the fluid-like behaviour required to explain
 507 isostatic rebound or convection in the mantle [O'Connell, 1971]. Yuen and Peltier [1982] pro-
 508 posed a Burgers rheology with a low transient viscosity ($\eta_K \approx 10^{16}$ Pa s) and high steady-
 509 state viscosity ($\eta_M \approx 10^{21}$ Pa s) to describe both seismic attenuation and long term geologic
 510 processes. The justification of a Burger's rheology mantle is further supported by laboratory
 511 experiments on olivine [Chopra, 1997]. Pollitz [2003] sought to describe postseismic defor-
 512 mation following Hector Mine with a Burgers rheology mantle and they found a best fitting
 513 transient viscosity of 1.6×10^{17} Pa s and steady-state viscosity of 4.6×10^{18} Pa s. While
 514 the Burgers rheology was introduced as a means of bridging the gap between relaxation ob-
 515 served in long and short term geophysical processes, the inferred steady state viscosity from
 516 Pollitz [2003] is still inconsistent with the Maxwell viscosities inferred from earthquake cy-
 517 cle and lake loading studies. The transient viscosity inferred by Pollitz [2003] is constrained
 518 by the earliest phase of postseismic deformation following the Hector Mine earthquake. While
 519 Pollitz [2003] ruled out deep afterslip as an alternative mechanism based on inconsistent ver-
 520 tical deformation, it is still possible to successfully describe all components of early postseis-
 521 mic deformation following the Hector Mine earthquake with afterslip at seismogenic depths
 522 [Jacobs *et al.*, 2002]. It is then possible that the preferred rheologic model from Pollitz [2003]
 523 was biased towards inferring a particularly low transient viscosity by neglecting to account for
 524 afterslip. This is in contrast to the present study, where we have inferred a lithospheric vis-
 525 cosity structure simultaneously with afterslip. We also argue that a transient rheology is nec-
 526 essary to explain postseismic deformation; however, our preferred transient viscosity of $\sim 10^{18}$
 527 Pa s in the mantle is an order of magnitude larger than the transient viscosity found by Pol-
 528 litz [2003]. Since a Zener model is able to describe the available postseismic deformation fol-
 529 lowing the El Mayor-Cucapah earthquake, any Burgers rheology with a steady-state viscous-
 530 ity that is $\gtrsim 10^{20}$ Pa s, effectively infinite over five years, would also be able to describe the
 531 postseismic deformation. Such a Burgers model might then be consistent with the steady state
 532 viscosities necessary for lake loading, interseismic deformation, and mantle dynamics.

533 5 Conclusion

534 We have extracted a filtered and smoothed estimate of postseismic deformation follow-
 535 ing the El Mayor-Cucapah earthquake from GPS displacements time series. We have treated
 536 postseismic deformation as a stochastic process where we did not presume any characteris-
 537 tic shape of the postseismic time series. We can observe transient postseismic deformation at
 538 distances of ~ 400 km from the El Mayor-Cucapah epicenter which is largely undetectable af-
 539 ter about three years. Near-field deformation exhibits transience that decays to a sustained, el-
 540 evated rate after about 1 to 2 year. We found that the near-field transient deformation can be
 541 explained with shallow afterslip and the sustained rate of near field deformation can either be
 542 explained with continued afterslip or relaxation in a lower crustal with a viscosity of $\sim 10^{19}$
 543 Pa s. Far-field transient deformation can be more definitively ascribed to viscoelastic relax-

544 at depths greater than \sim 60 km. Beneath that depth, a transient viscosity of \sim 10¹⁸ Pa s
 545 is required to describe the rate of far-field deformation throughout the five years considered
 546 in this study. By describing the available postseismic deformation with a transient rheology
 547 in the mantle, our preferred model does not conflict with the generally higher steady-state vis-
 548 cosities inferred from geophysical processes occurring over longer time scales.

549 Acknowledgements

550 We thank Andy Freed for an illuminating discussion on the data used in this study. This
 551 material is based on EarthScope Plate Boundary Observatory data services provided by UN-
 552 AVCO through the GAGE Facility with support from the National Science Foundation (NSF)
 553 and National Aeronautics and Space Administration (NASA) under NSF Cooperative Agree-
 554 ment No. EAR-1261833. This material is based upon work supported by the National Science
 555 Foundation under Grant Numbers EAR 1045372 and EAR 1245263.

556 References

- 557 Agaard, B. T., M. G. Knepley, and C. A. Williams (2013). A domain decomposition
 558 approach to implementing fault slip in finite-element models of quasi-static and dy-
 559 namic crustal deformation, *Journal of Geophysical Research: Solid Earth*, 118, doi:
 560 10.1002/jgrb.50217.
- 561 Argus, D. F., M. B. Heflin, G. Peltzer, F. Crampé, and F. H. Webb (2005), Interseismic
 562 strain accumulation and anthropogenic motion in metropolitan Los Angeles, *Journal of*
 563 *Geophysical Research: Solid Earth*, 110(4), 1–26, doi:10.1029/2003JB002934.
- 564 Aster, R. C., B. Borchers, and C. H. Thurber (2011), Parameter Estimation and Inverse
 565 Problems, vol. 90, Academic Press.
- 566 Bawden, G. W., W. Thatcher, R. S. Stein, K. W. Hudnut, and G. Peltzer (2001), Tectonic
 567 contraction across Los Angeles after removal of groundwater pumping effects., *Nature*,
 568 412(August), 812–815, doi:10.1038/35090558.
- 569 Bills, B. G., and G. M. May (1987), Lake Bonneville: Constraints on Lithospheric Thick-
 570 ness and Upper Mantle Viscosity From Isostatic Warping of Bonneville, Provo, and
 571 Gilbert Stage Shorelines, *Journal of Geophysical Research-Solid Earth and Planets*,
 572 92(B11), 11,493–11,508, doi:10.1029/JB092iB11p11493.
- 573 Çakir, Z., S. Ergintav, H. Özener, U. Dogan, A. M. Akoglu, M. Meghraoui, and
 574 R. Reilinger (2012), Onset of aseismic creep on major strike-slip faults, *Geology*,
 575 40(12), 1115–1118, doi:10.1130/G33522.1.
- 576 Cavalié, O., M. P. Doin, C. Lasserre, and P. Briole (2007), Ground motion measurement in
 577 the Lake Mead area, Nevada, by differential synthetic aperture radar interferometry time
 578 series analysis: Probing the lithosphere rheological structure, *Journal of Geophysical*
 579 *Research: Solid Earth*, 112(3), 1–18, doi:10.1029/2006JB004344.
- 580 Cetin, E., Z. Cakir, M. Meghraoui, S. Ergintav, and A. M. Akoglu (2014), Extent and
 581 distribution of aseismic slip on the Işmetpaşa segment of the North Anatolian Fault
 582 (Turkey) from Persistent Scatterer InSAR, *Geochemistry, Geophysics, Geosystems*, 15,
 583 doi:10.1002/2014GC005307. Received.
- 584 Chopra, P. N. (1997), High-temperature transient creep in olivine rocks, *Tectonophysics*,
 585 279, 93–111, doi:10.1016/S0040-1951(97)00134-0.
- 586 Crittenden, M. (1967), Viscosity and Finite Strength of the Mantle as Determined from
 587 Water and Ice Loads*, *Geophysical Journal of the Royal Astronomical ...*, pp. 261–279,
 588 doi:10.1111/j.1365-246X.1967.tb06243.x.
- 589 Davis, J. L., B. P. Wernicke, and M. E. Tamisiea (2012), On seasonal signals in geode-
 590 tic time series, *Journal of Geophysical Research: Solid Earth*, 117(1), 1–10, doi:
 591 10.1029/2011JB008690.
- 592 Feigl, K. L., and W. Thatcher (2006), Geodetic observations of post-seismic transients in
 593 the context of the earthquake deformation cycle, *Comptes Rendus - Geoscience*, 338,

- 594 1012–1028, doi:10.1016/j.crte.2006.06.006.
- 595 Fletcher, J. M., O. J. Teran, T. K. Rockwell, M. E. Osokin, K. W. Hudnut, K. J. Mueller,
 596 R. M. Spelz, S. O. Akciz, E. Masana, G. Faneros, E. J. Fielding, S. Leprince, A. E.
 597 Morelan, J. Stock, D. K. Lynch, A. J. Elliott, P. Gold, J. Liu-Zeng, A. González-
 598 Ortega, A. Hinojosa-Corona, and J. González-García (2014), Assembly of a large
 599 earthquake from a complex fault system: Surface rupture kinematics of the 4 April
 600 2010 El Mayor-Cucapah (Mexico) Mw 7.2 earthquake, *Geosphere*, 10(4), 797–827,
 601 doi:10.1130/GES00933.1.
- 602 Freed, A. M., R. Bürgmann, E. Calais, J. Freymueller, and S. Hreinsdóttir (2006), Impli-
 603 cations of deformation following the 2002 Denali, Alaska, earthquake for postseismic
 604 relaxation processes and lithospheric rheology, *Journal of Geophysical Research: Solid*
 605 *Earth*, 111, 1–23, doi:10.1029/2005JB003894.
- 606 Freed, A. M., R. Bürgmann, and T. Herring (2007), Far-reaching transient motions after
 607 Mojave earthquakes require broad mantle flow beneath a strong crust, *Geophysical*
 608 *Research Letters*, 34, 1–5, doi:10.1029/2007GL030959.
- 609 Gonzalez-Ortega, A., Y. Fialko, D. Sandwell, F. A. Nava-pichardo, J. Fletcher,
 610 J. Gonzalez-garcia, B. Lipovsky, M. Floyd, and G. Funning (2014), El Mayor-
 611 Cucapah (Mw7.2) earthquake: early near-field postseismic deformation from In-
 612 Sar and GPS observations, *Journal of Geophysical Research*, 119, 1482–1497, doi:
 613 10.1002/2013JB010193. Received.
- 614 Hauksson, E., J. Stock, K. Hutton, W. Yang, J. A. Vidal-Villegas, and H. Kanamori
 615 (2011), The 2010 Mw 7.2 El mayor-cucapah earthquake sequence, Baja California,
 616 Mexico and Southernmost California, USA: Active seismotectonics along the
 617 Mexican pacific margin, *Pure and Applied Geophysics*, 168(3918), 1255–1277, doi:
 618 10.1007/s00024-010-0209-7.
- 619 Hearn, E. H. (2003), What can GPS data tell us about the dynamics of post-seismic defor-
 620 mation ?, (2003), 753–777.
- 621 Hearn, E. H., S. McClusky, S. Ergintav, and R. E. Reilinger (2009), Izmit earthquake post-
 622 seismic deformation and dynamics of the North Anatolian Fault Zone, *Journal of Geo-*
623 physical Research: Solid Earth, 114(August 2008), 1–21, doi:10.1029/2008JB006026.
- 624 Hetland, E. A. (2003), Postseismic relaxation across the Central Nevada Seismic Belt,
 625 *Journal of Geophysical Research*, 108(Figure 2), 1–13, doi:10.1029/2002JB002257.
- 626 Hetland, E. A., and G. Zhang (2014), Effect of shear zones on post-seismic deformation
 627 with application to the 1997 Mw 7.6 manyi earthquake, *Geophysical Journal Interna-*
628 tional, 198, 259–269, doi:10.1093/gji/ggu127.
- 629 Hines, T. T., and E. A. Hetland (2013), Bias in estimates of lithosphere viscosity from
 630 interseismic deformation, *Geophysical Research Letters*, 40(16), 4260–4265, doi:
 631 10.1002/grl.50839.
- 632 Hines, T. T., and E. A. Hetland (2016), Rapid and simultaneous estimation of fault slip
 633 and heterogeneous lithospheric viscosity from post-seismic deformation, *Geophysical*
634 Journal International, 204(1), 569–582, doi:10.1093/gji/ggv477.
- 635 Jacobs, A., D. Sandwell, Y. Fialko, and L. Sichoux (2002), The 1999 (Mw7.1) Hector
 636 Mine, California, Earthquake: Near-Field Postseismic Deformation from ERS Interfer-
 637 ometry, *Bulletin of the Seismological Society of America*, 92(May), 1433–1442.
- 638 Johnson, K. M., and P. Segall (2004), Viscoelastic earthquake cycle models with deep
 639 stress-driven creep along the San Andreas fault system, *Journal of Geophysical Research*
640 B: Solid Earth, 109, 1–19, doi:10.1029/2004JB003096.
- 641 Johnson, K. M., R. Bürgmann, and J. T. Freymueller (2009), Coupled afterslip and vis-
 642 coelastic flow following the 2002 Denali Fault, Alaska earthquake, *Geophysical Journal*
643 International, 176(3), 670–682, doi:10.1111/j.1365-246X.2008.04029.x.
- 644 Jónsson, S., P. Segall, R. Pedersen, and G. Bjornsson (2003), Post-earthquake ground
 645 movements correlated to pore-pressure transients, *Nature*, 424(July), 179–183, doi:
 646 10.1038/nature01758.1.

- 647 Kaufmann, G., and F. Amelung (2000), Reservoir-induced deformation and continental
 648 rheology in vicinity of Lake Mead, Nevada, *Journal of Geophysical Research*, 105(B7),
 649 16,341, doi:10.1029/2000JB900079.
- 650 Kroll, K. A., E. S. Cochran, K. B. Richards-Dinger, and D. F. Sumy (2013), Aftershocks
 651 of the 2010 Mw 7.2 El Mayor-Cucapah earthquake reveal complex faulting in the Yuha
 652 Desert, California, *Journal of Geophysical Research: Solid Earth*, 118(October), 6146–
 653 6164, doi:10.1002/2013JB010529.
- 654 Lekic, V., S. W. French, and K. M. Fischer (2011), Lithospheric Thinning Beneath Rifted
 655 Regions of Southern California, *Science*, 334(November), 783–787.
- 656 Liu, H.-P., D. L. Anderson, and H. Kanamori (1976), Velocity dispersion due to anelastic-
 657 ity; implications for seismology and mantle composition, *Geophysical Journal Interna-*
 658 *tional*, 47(1), 41–58, doi:10.1111/j.1365-246X.1976.tb01261.x.
- 659 Lundgren, P., E. A. Hetland, Z. Liu, and E. J. Fielding (2009), Southern San Andreas-San
 660 Jacinto fault system slip rates estimated from earthquake cycle models constrained by
 661 GPS and interferometric synthetic aperture radar observations, *Journal of Geophysical*
 662 *Research: Solid Earth*, 114(2), 1–18, doi:10.1029/2008JB005996.
- 663 McGuire, J. J., and P. Segall (2003), Imaging of aseismic fault slip transients recorded
 664 by dense geodetic networks, *Geophysical Journal International*, 155(3), 778–788, doi:
 665 10.1111/j.1365-246X.2003.02022.x.
- 666 Meade, B. J., and B. H. Hager (2005), Block models of crustal motion in southern Cal-
 667 ifornia constrained by GPS measurements, *Journal of Geophysical Research B: Solid*
 668 *Earth*, 110, 1–19, doi:10.1029/2004JB003209.
- 669 Murray, J. R., and P. Segall (2005), Spatiotemporal evolution of a transient slip event on
 670 the San Andreas fault near Parkfield, California, *Journal of Geophysical Research : Solid*
 671 *Earth*, 110(9), 1–12, doi:10.1029/2005JB003651.
- 672 Nur, A., and G. Mavko (1974), Postseismic viscoelastic rebound, *Science*, 183(4121),
 673 204–206, doi:10.1038/098448b0.
- 674 O'Connell, R. J. (1971), Rheology of the Mantle, *EOS, Transactions, American Geophysi-*
 675 *cal Union*, 52, 140–142.
- 676 Oskin, M. E., J. R. Arrowsmith, A. Hinojosa Corona, A. J. Elliott, J. M. Fletcher, E. J.
 677 Fielding, P. O. Gold, J. J. Gonzalez Garcia, K. W. Hudnut, J. Liu-Zeng, and O. J. Teran
 678 (2012), Near-field deformation from the El Mayor-Cucapah earthquake revealed by
 679 differential LIDAR, *Science*, 335(6069), 702–705, doi:10.1126/science.1213778.
- 680 Pollitz, F., C. Wicks, and W. Thatcher (2001), Mantle Flow Beneath a Continental Strike-
 681 Slip Fault : Postseismic Deformation After the 1999 Hector Mine Earthquake, *Science*,
 682 1814(2001), 1814–1818, doi:10.1126/science.1061361.
- 683 Pollitz, F. F. (2003), Transient rheology of the uppermost mantle beneath the Mo-
 684 jave Desert, California, *Earth and Planetary Science Letters*, 215, 89–104, doi:
 685 10.1016/S0012-821X(03)00432-1.
- 686 Pollitz, F. F., G. Peltzer, and R. Bürgmann (2000), Mobility of continental mantle: Evi-
 687 dence from postseismic geodetic observations following the 1992 Landers earthquake,
 688 *Journal of Geophysical Research*, 105(1999), 8035, doi:10.1029/1999JB900380.
- 689 Pollitz, F. F., R. Bürgmann, and W. Thatcher (2012), Illumination of rheological mantle
 690 heterogeneity by the M7.2 2010 El Mayor-Cucapah earthquake, *Geochemistry, Geo-*
 691 *physics, Geosystems*, 13(6), 1–17, doi:10.1029/2012GC004139.
- 692 Rauch, H. E., F. Tung, and C. T. Striebel (1965), Maximum likelihood estimates of linear
 693 dynamic systems, *AIAA Journal*, 3(8), 1445–1450.
- 694 Riva, R. E. M., and R. Govers (2009), Relating viscosities from postseismic relaxation to
 695 a realistic viscosity structure for the lithosphere, *Geophysical Journal International*, 176,
 696 614–624, doi:10.1111/j.1365-246X.2008.04004.x.
- 697 Rollins, C., S. Barbot, and J.-P. Avouac (2015), Postseismic Deformation Following the
 698 2010 M7.2 El Mayor-Cucapah Earthquake : Observations , Kinematic Inversions , and
 699 Dynamic Models, *Pure and Applied Geophysics*, doi:10.1007/s00024-014-1005-6.

- 700 Savage, J. C. (1990), Equivalent strike-slip earthquake cycles in half-space and
701 lithosphere-asthenosphere earth models, *Journal of Geophysical Research*, 95, 4873,
702 doi:10.1029/JB095iB04p04873.
- 703 Savage, J. C., and J. L. Svart (2009), Postseismic relaxation following the 1992 M 7.3
704 Landers and 1999 M 7.1 Hector Mine earthquakes , southern California, *Journal of*
705 *Geophysical Research*, 114(B01401), doi:10.1029/2008JB005938.
- 706 Savage, J. C., J. L. Svart, and S. B. Yu (2005), Postseismic relaxation and transient creep,
707 *Journal of Geophysical Research: Solid Earth*, 110, 1–14, doi:10.1029/2005JB003687.
- 708 Segall, P., and M. Mathews (1997), Time dependent inversion of geodetic data, *Journal of*
709 *Geophysical Research*, 102.
- 710 Spinler, J. C., R. A. Bennett, C. Walls, L. Shawn, and J. J. G. Garcia (2015), As-
711 sessing long-term postseismic deformation following the M7.2 4 April 2010, El
712 Mayor-Cucapah earthquake with implications for lithospheric rheology in the
713 Salton Trough, *Journal of Geophysical Research: Solid Earth*, 120, 3664–3679, doi:
714 10.1002/2014JB011613.Received.
- 715 Wei, M., D. Sandwell, Y. Fialko, and R. Bilham (2011a), Slip on faults in the Imperial
716 Valley triggered by the 4 April 2010 Mw 7.2 El Mayor-Cucapah earthquake revealed by
717 InSAR, *Geophysical Research Letters*, 38(January), 1–6, doi:10.1029/2010GL045235.
- 718 Wei, M., Y. Liu, Y. Kaneko, J. J. McGuire, and R. Bilham (2015), Dynamic triggering of
719 creep events in the Salton Trough, Southern California by regional M5.4 earthquakes
720 constrained by geodetic observations and numerical simulations, *Earth and Planetary*
721 *Science Letters*, 427, 1–10, doi:10.1016/j.epsl.2015.06.044.
- 722 Wei, S., E. Fielding, S. Leprince, A. Sladen, J.-P. Avouac, D. Helmberger, E. Hauksson,
723 R. Chu, M. Simons, K. Hudnut, T. Herring, and R. Briggs (2011b), Superficial sim-
724 plicity of the 2010 El MayorCucapah earthquake of Baja California in Mexico, *Nature*
725 *Geoscience*, 4(9), 615–618, doi:10.1038/ngeo1213.
- 726 Yuen, D. A., and W. R. Peltier (1982), Normal modes of the viscoelastic earth, *Geo-*
727 *physical Journal of the Royal Astronomical Society*, 69, 495–526, doi:10.1111/j.1365-
728 246X.1982.tb04962.x.